Bright X-ray Stainless Steel K-shell Source Development at the National Ignition Facility

M. J. May, K. B. Fournier, J. D. Colvin, M. A. Barrios, E. Dewald, M. Hohenberger, J. Moody, J. R. Patterson, M. Schneider, K. Widmann, S. P. Regan

February 23, 2015

LAWRENCE
LIVERMORE
NATIONAL
LABORATORY

Disclaimer

This document was prepared as an account of work sponsored by an agency of the United States government. Neither the United States government nor Lawrence Livermore National Security, LLC, nor any of their employees makes any warranty, expressed or implied, or assumes any legal liability or responsibility for the accuracy, completeness, or usefulness of any information, apparatus, product, or process disclosed, or represents that its use would not infringe privately owned rights. Reference herein to any specific commercial product, process, or service by trade name, trademark, manufacturer, or otherwise does not necessarily constitute or imply its endorsement, recommendation, or favoring by the United States government or Lawrence Livermore National Security, LLC. The views and opinions of authors expressed herein do not necessarily state or reflect those of the United States government or Lawrence Livermore National Security, LLC, and shall not be used for advertising or product endorsement purposes.

Bright X-ray Stainless Steel K-shell Source Development at the National Ignition Facility

M. J. May,[1] K. B. Fournier,[1] J. D. Colvin,[1] M. A. Barrios,[1] E. L. Dewald,[1] M. Hohenberger,[2] J. Moody,[1] J. R. Patterson,[1] M. Schneider,[1] K. Widmann,[1] and S. P. Regan[2]

[1]*PO Box 808 L260, Lawrence Livermore National Laboratory, Livermore CA 94551.*

[2]*Laboratory for Laser Energetics, University of Rochester, Rochester NY 14623.*

(Dated: June 1, 2015)

Abstract

High x-ray conversion efficiency (XRCE) K-shell sources are being developed for High Energy Density (HED) experiments for use as backlighters and for the testing of materials exposed to high x-ray fluxes and fluences. Recently, sources with high XRCE in the K-shell x-ray energy range of iron and nickel were investigated at the National Ignition Facility. The x-ray conversion efficiency in the 5 - 9 keV spectral range was determined to be $6.8\pm0.3\%$. These targets were 4.1 mm diameter, 4 mm tall hollow epoxy tubes having a 50 μm thick wall supporting a tube of 3 to 3.5 μm thick stainless steel. The NIF laser deposited $\sim$460 kJ of 3ω light into the target in a 140 TW, 3.3 ns square pulse. The absolute x-ray emission of the source was measured by two calibrated Dante x-ray spectrometers. Time resolved images filtered for the Fe K-shell were recorded to follow the heating of the target. Time integrated high-resolution spectra were recorded in the K-shell range.

I.   INTRODUCTION

Bright multi-keV x-ray sources (E_{photon} = 1 - 20 keV) have been under development for more than the past 10 years [1] and are needed for a variety of inertial confinement fusion (ICF) [2] and high energy density (HED) [3] research applications. Significant efforts to create these bright, multi-keV x-ray sources exist at pulsed power facilities such as the Z machine at the Sandia National Laboratories [4] and at high power laser facilities such as the OMEGA laser [5] at the Laboratory for Laser Energetics and at the National Ignition Facility (NIF) [6, 7] at the Lawrence Livermore National Laboratory. These x-ray sources are useful as backlighters for imaging and radiography applications in ICF implosions and laser-driven shock experiments [8–11]. Also, high fluence, broad band sources are needed for studies of x-ray interaction with materials [12]. Large, homogeneous sources can be used for area backlighters [13], and very bright small sources are apertured for point-projection backlighters [14–16]. Maximizing the laser to x-ray conversion efficiency (XRCE) and tuning the spectral content of the x-ray source are crucial to satisfy the requirements of a given application.

For the laser experiments [1, 17–27], the goal has been to create homogeneous, keV temperature plasmas that maximize the XRCE in a given spectral region. Traditionally, laser-irradiated foils were used as x-ray sources for these experiments. However, the high-density plasma generated during the ablation of the solid planar targets prevents the laser from fully penetrating the target material and limits the XRCE to only a fraction of a percent in the K-shell [28]. The XRCE was significantly increased by using targets that create underdense plasmas, which are plasmas with an electron density below $\sim$0.25n_c. The critical density, n_c, is $1.1 \times 10^{21}/[\lambda(\mu m)]^2 \sim 1 \times 10^{22}$ cm^{-3} for 3ω (λ = 0.351 μm) laser light. In these underdense plasmas, the heat front can propagate supersonically through the target [29], which allows full volumetric heating of the emitting material. The underdense plasma is heated faster than one would expect by ordinary thermal conduction processes and heated faster than the plasma can cool by adiabatic expansion at the sound speed. Therefore, a larger fraction of the target material is ionized to the appropriate charge states to produce greater XRCE. In these underdense targets, the XRCE for photon energies > 2 keV have been measured to be 1% to 10% using pre-exploded foils [24, 30], metal-doped aerogels [19, 22, 33], metal oxide nanofibers [23], and gas-filled [21, 31, 34] targets. Cylindrically shaped targets,

which confine and allow further heating of low-density plasmas ablated from solid target walls, can also substantially increase the XRCE. Foil-lined hohlraums demonstrated XRCEs of up to 7% [26, 32, 33].

The creation of optimal XRCEs in mid- to high-Z x-ray sources is challenging at laser facilities due to the limited total power and energy available. Calculations show that the multi-keV emissivity of highly charged mid-Z ions in a plasma is a strong function of temperature [34]. The optimum temperature is different for each element and emission line. With the available laser energy, the achievable plasma temperatures have not necessarily been matched to the temperature required for the optimal multi-keV x-ray emissivity. Higher electron temperatures are now achievable using the NIF [6, 7] laser which can deliver ~ 1.8 MJ of laser energy in < 15 ns to heat these x-ray sources. The first multi keV x-ray laser-heated targets at NIF were created with Xe/Ar gas pipes [31]. An XRCE of $13\pm1.3\%$ for photon energies > 3 keV was reported.

In this paper, the results of NIF experiments are presented that characterize cylindrical stainless steel 304 (SS-304) x-ray sources, and, in particular, their emission in the Cr, Fe, and Ni K-shell energy band (5.0 to 9.0 keV). In these experiments, 4.1 mm diameter and 4 mm tall epoxy tubes lined with 3.0 to 3.5 μm thick SS-304 were heated with the NIF laser. The laser deposited $\sim$460 kJ of energy at an average power of $\sim$140 TW in a 3.3 ns square pulse in time. A suite of NIF diagnostics was used to record the x-ray and the visible emission from the target during the experiments (Figure 1). The XRCE and the temporal behavior of the target heating were well characterized. The time evolution of the x-ray absolute radiant intensity was measured by using the Dante 1 and Dante 2 low resolution spectrometers [35, 37, 54] . The volumetric evolution of the Fe, Ni and Cr K-shell emission was recorded by an appropriately filtered pinhole imager mounted on one of NIFs gated x-ray cameras (hGXI) [38]. Full-Aperture Backscatter (FABS) [39] and Near Backscatter Imaging (NBI) [40] systems quantified the incident laser light reflected from the target in the optical. The scattering from ion-acoustic waves (stimulated Brillouin scattering (SBS)) and from plasma-electron waves (stimulated Raman scattering (SRS)) was 30 to 45 kJ or 7 to 10% of the input laser energy. Time integrated, high resolution spectra of the Fe, Cr and Ni K-shell ions were recorded in the 6 - 10 keV spectral region by an elliptically bent crystal spectrometer [41].

The XRCE from the SS-304 target was determined to be $6.8\pm0.3\%$ in the 5 - 9 keV

spectral range from the Dante measurements. For this estimate the source is assumed to emit isotropically in the 5 - 9 keV spectral range. This is a significant increase from the XRCE reported by Pérez *et al.* for smaller cylindrical SS-304 targets shot at the OMEGA laser facility [33]. Pérez *et al.* utilized 20 kJ in a 1 ns laser pulse and reported XRCE's of 1.6 - 2.2% in the K-shell energy range. The higher conversion efficiency at NIF is a result of the substantially larger available laser energy. The targets shot at NIF were heated to a much higher peak electron temperature ($\sim$7 keV), which is much nearer to that required for optimal XRCE of the iron K-shell.

II.   LASER DRIVE

The NIF laser was used to irradiate four targets for the measurements presented here. The NIF is a 192 beam laser system, which is capable of delivering more than 1.8 MJ of 3ω (351 nm) laser energy into millimeter scale targets positioned at the center of a $\sim$10 m in diameter target chamber. For this work, a total of 160 beams could be used with the laser and target geometry. However, the total number of beams on a given shot was limited by the system availability. This meant that the targets were heated with either 152 (for only N140221-001) or 156 beams (for the other three shots). The laser power and number of quads (groups of 4 beams) used for each shot are summarized in Table I. The measured and intended laser powers are shown in Figure 2. A total of $\sim$460 kJ of energy ($\sim$3.125 kJ/beam) was delivered to each target with an average power of $\sim$145 TW. The power in each of the 152 beams for N140221-001 was increased by about 1.02 times to compensate for one of the lost quads. This maintained the same total power and total energy for all four of the shots. The loss of one or two of the quads did not significantly affect drive symmetry.

The requested laser pulse was nominally a 3.3 ns long pulse. All the beams were ramped up to full power in a rise time of 200 - 250 ps. The delivered laser power had a nominal constant power in the flat top with a slight maximum at 1.5 ns. The lasers were ramped down to zero power in about 200 - 250 ps. The total delivered energy at the target chamber center (TCC) was about 8% below the intended energy.

The 192 beams in the NIF are grouped in sets of 48 quads. The 48 quads are clustered in four separate beam cones. The NIF laser beams enter the chamber in these four cones that have azimuthal symmetry around the vertical axis of the target chamber. The beam cones

propagate to TCC with angles of 23.5°, 30°, 44.5°, and 50° from the chamber vertical. Half the beams in each cone come from the top of the NIF target chamber, while the other half come from the bottom. The 23.5° and 30° beams collectively are referred to as the inner cone and the 44.5° and 50° beams are collectively referred to as the outer cone.

Each cylindrical target was positioned so that its center was at the NIF TCC and was oriented so that the cylindrical axis was vertical in the chamber. All the beams were pointed so that their spots terminated on the inside wall of each target. For these experiments, the beams used to heat the target were from the eight quads at 30°, the sixteen quads at 44.5° and the sixteen quads at 50° (Figure 1). The eight 23.5° inner cones were not used since the projection of the beam spot onto the target was larger than the 4 mm tall target wall.

About 20% of the power was provided by the inner cones; the rest came from the outer cones. The outer cone beams crossed at 0.5 mm inside the laser entrance holes (LEHs) (1.5 mm from the target center) creating an intensity for the 64 outer cone beams at each LEH of $\sim$3.125 (kJ/beam) / 0.01 (cm^2) / 3.3 (ns) * 64 = 9.5x10^{13} (W/cm^2) * 64 = 6x10^{15} (W/cm^2). The 16 inner cone beams crossed at 0.8 mm outside the LEH (2.8 from the target center) with an intensity of $\sim$3.125 (kJ/beam) / 0.02 (cm^2) / 3.3 (ns) * 16 $\sim$4.7x10^{13} (W/cm^2) * 16 $\sim$7x10^{14} (W/cm^2).

High power lasers can typically have significant non-uniformities in the beam spatial profiles. This is undesirable since these non-uniformities can increase the backscatter of laser light into the optics, which will reduce the delivered energy onto the target or damage the optics. The non-uniformities potentially can cause irregular heating of the target surfaces. These effects can reduce the XRCE. For the experiments presented in this work, the variation in intensity across each beam's spatial profiles was mitigated by several beam smoothing techniques. Continuous phase plates, CPPs, which expanded the focal spots and smoothed the intensity distribution within the spot, were installed in each beam line [42, 43]. The outer cone phase plates created elliptical spots of approximately 1200 μm by 700 μm at best focus. The inner cone CPPs created a larger spot of approximately 1700 μm by 1200 μm. These spots are effectively a circle when projected onto the plane of each of the cylinder ends. The CPPs parameters are summarized in Table II. Smoothing by spectral dispersion bandwidth was applied to the laser seed pulse from the master oscillator at a frequency of 45 GHz. Additionally, differential polarization rotation crystals were in each beam path. In each of the NIF quads, two of these rotation crystals were oriented with their polarization

5

vertical, and two were oriented horizontal. This separated orthogonal polarizations of each beam and overlapped them at the position of best focus, which reduced the intensity of the hot spots by $\sqrt{2}$.

III. STAINLESS STEEL TARGETS

The targets used in the NIF experiments were fairly simple in construction. The targets were thin walled cylindrical tubes made of epoxy ($C_{40}H_{51}N_2O_7$) having a density, ρ, of 1.185 g/cm^3 and with an inside diameter of 4.1 mm and a length of 4 mm. The targets had no end caps with the laser entrance hole (LEH) being the full diameter of the tube. The 50 μm thick walls of the tubes were specifically chosen to both maximize the transmission of the Fe, Ni and Cr K-shell x-rays, to produce an isotropic source between E_{photon} = 5 - 9 keV. A 3.0 to 3.5 μm thick coating of SS-304 was sputtered onto a mandrel. The SS-304 had atomic percentages of 70% Fe, 17% Cr, 9% Ni, 1% Mo, 1.5% Si and 1.5% Mn. The epoxy tube was coated onto the SS-304 layer and back machined to 50 μm thick walls. The mandrel was disolved away. The metrology data for each of these targets are given in Table III.

The SS-304 thickness and mass were chosen to maximize the Fe, Ni and Cr K-shell emission by making the heated plasma underdense. The optimal electron density to maximize the target XRCE should be $\sim$0.25 n_c or $\sim$2.5x10^{21} electrons/cm^3. If the target density is much higher than about $\sim$0.25 n_c, the LPI losses increase and reduce the laser absorption and the target XRCE. Since the the x-ray emission is proportional to n_e^2, the final target density should be as high as possible without causing significant LPI. This sub-critical density is close to optimum for these targets. The 3.3 ns laser pulse fully ablates the SS-304 coating on the inside of the epoxy tube, which then expands into the volume tamped by the tube to become an underdense homogeneous plasma. The mass of a 3.5 μm SS-304 coating was $\sim$0.014 g assuming a solid density of 8.0 g/cm^3. The target volume was $\sim$0.5 cm^3, which makes the SS-304 plasma density $\sim$7 mg/cm^3. Assuming all the SS-304 is close to being fully ionized in the target, the electron density is just under the quarter critical density.

One critical requirement for the bright x-ray source is a stable and repeatable K-shell emission from one target to the next. Stainless steel cavity targets and low density (3 - 10 mg/cm^3) $FeO_2HCl_{0.38}$ aerogel targets were considered as potential bright x-ray sources for use on the NIF. Simulations of the NIF targets predicted that 6 mg/cm^3 aerogel targets

6

should have about 2 times the K-shell emission of the SS-304 cavity targets. From the experiments [33] on OMEGA, the low density aerogel targets have been shown to have, on average, a slightly higher XRCE, in the K-shell than the SS-304 cavity targets. The SS-304 cavity targets had a very repeatable XRCE which was not significantly affected by the 0.5 μm variation of the SS-304 coating from target to target. However, the aerogels targets were found to have significant variations in the yield which made them less ideal for the NIF experiments. The variations in the XRCE from the aerogels targets is most likely due to density non-uniformities and gradients in the aerogels resulting from the manufacturing process.

IV. SIMULATIONS

The laser heating of the target and its subsequent radiation in the 0.1 to 10 keV spectral range was simulated prior to the experiments. This was done to guide the design of the target, to optimize the emission in the K-shell and to assist in the setup of the measurement diagnostics for the experiment. Significant effort was applied to calculate accurately the emission spectrum from the target. Since the sub-critical-density plasma created by the laser beam illumination is not in local thermodynamic equilibrium (LTE) - that is, the ion and electron collision processes do not dominate the energy exchange - an accurate calculation of the x-ray emission is needed to account for all of the atomic transition processes that affect the ionization balance in the plasma. This can be done by solving a large set of rate equations, one for each possible energy exchange transition between free electrons, bound electrons, and photons. This potentially could be a very large number of transitions included in the radiation-hydrodynamics simulation. Complete detailed accounting of all these transitions do not need to be included in the model for good accuracy. A very good approximation to the full calculation defines super-configurations that consist of several quantum energy levels that are relatively close together in energy, and then solve the non-LTE rate equations for the much smaller set of transitions to and from the super-configurations. This method is a good balance between accuracy of the spectrum and computational tractability. Such a super-configuration model, called DCA, was previously developed and incorporated into the 2D radiation-hydrodynamics code LASNEX [44] by Scott and Hansen [45].

The DCA model solves the rate equations to obtain the populations of each energy level

7

of each ionization stage. A principal quantum number description is used that includes 10-20 quantum energy levels per ionization stage. The model calculates the screened-hydrogenic energy levels and rates; includes doubly-excited and auto-ionizing states, tabulated ionization energies, and tabulated $\Delta n = 0$ transitions (for radiative properties). The calculation of line shapes includes Stark, Doppler and configuration broadening.

LASNEX is a 2D radiation-hydrodynamics code in which the equations of motion for the plasma are solved in the Lagrangian formulation. A specially designed automatic rezoning routine was written for this particular target simulation to avoid tangling of the moving mesh as the SS-304 plasma fills the can and converges on axis. After a certain time the simulations are switched to an Eulerian formulation by freezing the mesh in place. Laser beam propagation is followed with a 3D ray-tracing algorithm, with beam energy absorbed by inverse bremsstrahlung as the beam propagates through the under-dense plasma. A key feature of the model is that electron thermal conduction is treated in the Spitzer-Harm formulation [46] with a flux limiter of 0.2 to account for non-local thermal transport.

The LASNEX/DCA model was previously benchmarked to data from OMEGA laser [5] shots of Ge doped silica aerogel targets [47] and data from the 2009 NIF shots of Ar/Xe x-ray source gas pipes [48]. The same computational model was used for NIF SS-304 targets that are the subject of this paper. In these simulations a new DCA model was specially constructed for Fe, with 887 super-configurations. It also included super-configuration models for the other constituents of the SS-304 lining the epoxy tube. The LASNEX results presented included the actual laser pulse and the final target metrology.

V. X-RAY INTENSITY MEASUREMENTS

The time evolution of the x-ray spectral emission was measured by using the two NIF Dante spectrometers [37, 54]. A Dante is a low resolution diode spectrometer that is commonly used for hohlraum drive measurements in inertial fusion experiments. The emitted radiation from a laser heated target is recorded by 18 separately filtered channels with a temporal resolution of $\sim$150 ps. Each channel is configured to record a specific but different broad x-ray spectral band between 0.05 to 20 keV. A different set of x-ray filters, mirrors and x-ray diodes (XRDs) is used in each channel to optimize the measurement of each spectral region. Absolute radiant intensity measurements are possible since all components are

absolutely calibrated, and the geometry of the system is known. The time resolved x-ray spectra are determined from the recorded channel voltages by using a spectral reconstruction algorithm, typically called an unfold, and the photometric response of each channel.

The Dante 1 and 2 components (e.g. using the same filters, XRDs, etc.) were not changed between the first set of two target shots (N120627-002 and N120628-001) as well as the second set of two shots (N140220-002 and N140221-001). The configuration between the first and second set of shots was nominally the same but had a different set of components. A typical Dante 1 configuration is given in Table IV. The Dante 2 configuration was very similar but lacked several channels in the 3 - 5 keV spectra region. The radiant energy and XRCE from the target in the x-ray ranges that were determined by the Dante spectrometers are summarized in Table V.

The Dante 1 and 2 are positioned on the NIF target chamber at $\theta=143°;\phi=274°$ and $\theta=64°;\phi=350°$, respectively. The Dante 1 and 2 observed each target at 37° and 64°, respectively, from the target's cylindrical axis. The different views of the target are utilized to interpret the angular variation of the emission. The targets are assumed to have azimuthally symmetric emission. This is a reasonable assumption since the targets are cylindrical in nature and the laser beams from NIF have azimuthal symmetry. The emission from the targets, however, varied as a function of polar angle from the cylindrical axis. The construction of the target complicated this by making the angular variation a function of photon energy. The 50 μm thick epoxy tube absorbs much of the low energy photons and $< 5\%$ transmission for photon energies, E_{photon}, below $\sim$3 keV. Above E_{photon} $\sim$3 keV, the target wall has $>$ 80% transmission. The M- and L-shell emission from Fe, Ni and Cr will have a significant angular dependence, whereas, the K-shell emission will be nearly isotropic.

The total x-ray radiant intensity (summed over 0.05 - 20 keV) from the reconstructed Dante 1 and 2 spectra are shown in Figure 4 for N120627-002 and N140220-002. The time histories for shots N120628-001 and N140221-001 are very similar and are not shown for clarity. Also plotted are the laser powers for both shots. The lasers heat the SS-304 on the inside of the epoxy tube through the process of inverse bremsstrahlung. The x-ray emission increases as a result of the heating and peaks at 3 ns just before the laser pulse ends. The x-rays continue to emit for 4 - 5 ns after the lasers turned off as the SS-304 plasma cools and recombines. The total Dante 1 x-ray radiant intensities are fairly consistent for all four shots. The total Dante 2 x-ray radiant intensities in the second set of experiments were a

bit less than in the first set and outside the error bars of the Dante measurements [49].

The time evolutions of the radiation from Dante 1 and 2 are very similar, however, the absolute magnitude from Dante 1 was about 1.8 times of that recorded by the Dante 2. The difference is due to the < 3 keV emission. This can be seen in the total reconstructed spectra, which are plotted in Figure 5 for both Dante spectrometers for shots N120627-002 and N140220-002. The spectra from shots N120628-001 and N140221-001 are very similar and are not shown for clarity. The one sigma uncertainties from the spectral reconstruction are plotted for the Dante 1 from N120627-002 in Figure 6. The majority of the emission below 3 keV is from the M-shell and L-shell ions in the stainless steel (e.g. Fe, Ni, Cr, etc.). The epoxy wall is fairly opaque to these photon energies, but does get heated and radiates like a 50 to 100 eV blackbody. The target images from the OMEGA experiments (see figure 2 in Ref [50]) have not recorded significant x-ray emission (E_{photon} ~250 eV and 450 eV) from the walls. We assume that most of the < 3 keV emission is radiated from the two LEHs for the NIF targets.

The obvious question is whether or not the LEHs are Lambertian radiators below 3 keV. A Lambertian surface has the same radiance (W/steradian/area) when viewed from any angle. The LEH images from the OMEGA experiments (Ref [50]) have been observed to be a uniformly emitting disk. If the tube ends are a Lambertian source then the radiant intensity can be written as I = I_0cos(θ) dω dA. I_0 is the radiant intensity when viewing the disks normal to the surface and θ is measure from the normal. Dante 1 and 2 are at $\theta = 37°$ and 64° from the cylinder axis, respectively. The ratio of cos(37°)/cos(64°) = 1.82, which is nominally the difference in the sub 3 keV emission recorded at the two different Dante angles. This is consistent with the tube ends being Lambertian-like sources. Assuming a Lambertian source, one can estimate the total radiant intensity from each of the LEHs, I_0. The radiant energy below 3 keV is corrected by 1/cos(37°) = 1.25 and 1/cos(64°) = 2.28 for Dante 1 and Dante 2, respectively to give the total emitted energy (Table V).

The K-shell features from Cr, Ni and Fe are seen in the reconstructed spectra between 5 - 9 keV in Figure 5. The K-shell time evolution is very consistent for all four shots and is shown in Figure 7. The K-shell emission decayed quickly since the high temperatures needed to support this emission could not be sustained once the laser heating ended. The K-shell radiant intensity is isotropic as inferred from the different views of each Dante.

The LASNEX predicted x-ray radiant intensity for Dante 1 versus time is compared with

the measurement for shot N120627-002 in Figure 8. The modeling does not fully reproduce the measurements. The major discrepancy is at the peak of the total emission where the modeling is ~20% greater than the measurement. The K-shell comparison is also shown in the figure for photon energies between 5 - 9 keV. The comparison is reasonable when the total K-shell emission from all the elements (e.g. Cr, Fe and Ni) is included. However, the simulations are slightly less than the experiment.

Some additional insight can be gained by comparing the LASNEX and the measured spectra. The LASNEX high resolution spectra can be processed to produce a synthetic reconstructed Dante spectra. The LASNEX high resolution spectra is sent through the actual Dante instrument response (e.g. filter, solid angle, etc.) to generate simulated time dependent voltages for each of the 18 XRDs of Dante. These simulated voltages were then processed by the Dante reconstruction algorithm in the identical manner as the measured voltages to generate a synthetic Dante spectrum. This also serves as a consistency check on the Dante spectral reconstruction. Robey *et al.* has done a detailed investigations that validates the use of Dante for this type of measurement. [51] The synthetic and measured Dante 1 spectra for target shot N120627-002 are compared in Figure 9. The agreement between the two spectra is very good. The major difference between the modeling and the experiment is in the K-shell Fe emission. The LASNEX simulation underestimates the K-shell emission by about a factor of 2. This disagreement for individual K-shell lines has been observed previously [31, 34] and is discussed in detail below.

VI.   K-SHELL X-RAY IMAGING

The targets were imaged during the laser heating to quantify the temporal evolution of the volumetric emission. A simple pinhole camera geometry was used to record images with a side-on or equatorial view of the target. The imaging snout containing the pinholes and filters was mounted to one of NIFs gated x-ray detectors [38], hGXI, located in the 90-78 equatorial diagnostic instrument manipulator (DIM). The hGXI is a four strip gated microchannel plate (MCP) x-ray detector. A phosphor is used to convert the MCP electrons to visible light for recording on photographic film.

The imaging snout had a magnification of 1 with a detector to target distance of 1280 mm. Sixteen separate images were recorded through sixteen 25 μm in diameter pinholes

that were mounted in a square array. Four images were recorded on each of the MCP/film strips, which are about 36 mm in length and 7.5 mm tall. The spatial resolution of the MCP is about 75 μm, which limits the resolution of the image.

Each MCP strip was independently gated to record images at different times during shots N120627-002 and N120628-001. No images were taken on N140220-002 and N140221-001. The timing, t_{strip}, of each GXD strip was 1.03, 2.04, 3.10, and 4,15 ns for shot N120627-002 and 0.94, 1.97, 3.03, and 4.08 ns for shot N120628-001. The t_{strip} was referenced from the center of the MCP. The width of the high voltage electrical gating pulse was about 200 ps which gives the camera a temporal resolution for the x-rays of about 100 ps. The transit time of the electrical pulse across the plate was 250 ps.

Each hGXI MCP strip has a low and a high gain region. The gain of the MCP varies across the surface by about a factor of 2. The strip gain is highest at the beginning of the pulse and spreads in time slightly and drops in gain as it propagates across the strip. Two different filters were used to adjust the signal levels on the film to be roughly constant along the MCP strip. The high gain side of the MCP was filtered with 25 μm of Fe. The low gain side was filtered with 12.5 μm of Fe. With this filtering, the target was imaged in 5.5 - 7.11 keV x-rays. The emission in the filter bandpass is mainly the H-like (2→1) and the He-like (2→1) transitions of K-shell Fe with some emission from higher n Cr K-shell lines.

One image from each of the four strips is plotted in Figure 10 for N120627-002 and N120628-001 along with the simulated images from the LASNEX calculations. These experimental images are corrected for the film's logarithmic sensitivity, the MCP gain variation and the filter transmission. These images have a relative, not an absolute, photometric calibration. The alignment of the imaging snout was not perfect. Therefore, the recorded images at 3 and 4 ns are slightly clipped on the right which is the edge of the MCP.

One can see that the predicted LASNEX images are in fair qualitative agreement with experiment. The spatial resolution of the measured images is high enough to capture only the global evolution seen in the simulated images. The finer structure seen in the simulated images cannot be resolved by the current imager. The K-shell emission evolves as a function of time. At 1 ns the lasers have just started to heat the target. The SS-304 layer on the target wall has been heated enough to start radiating in a uniform band at the waist of the target where the lasers terminate. At 2 ns, the heated plasma has filled the inside of the epoxy tube. Also, the ablated SS-304 has collided at the center of the target. The plasma

stagnation can be seen as the central column. At 3 ns the stagnation region has expanded into the material that is still being ablated from the walls. The target was volumetrically heated and is a uniformly emitting cylinder of K-shell radiation. The x-ray emission is brightest in this frame and consistent with the Dante measurements. At 4 ns, the K-shell emission continues to radiate uniformly as the target cools and recombines.

VII. HARD X-RAY EMISSION

The hard x-ray spectra ($h\nu > 20$ keV) were measured with the filter-fluorescer diagnostic system, FFLEX [52–54]. Hot electrons are the major contributor to the hard x-ray spectra. This emission is small and does not contribute much to the total emission, but is included for completeness. Ten FFLEX channels are configured to measure a specific hard x-ray energy with a narrow photon energy range. The lowest and highest energy channels record x-rays around ~20 and ~240 keV, respectively. Figure 11 shows the hard x-ray data from each of the FFLEX channels and the fitted spectra to the data for the four target shots. The bremsstrahlung emission, I, was fit assuming a single Maxwell-Boltzmann electron temperature, T_{hot}, with the formula [55]:

$$I \left[\frac{keV}{keV \cdot sr} \right] = \frac{5x10^{11}}{4\pi} \frac{<Z>}{79} E_{hot} \left(1 - exp \left(\frac{h\nu}{T_{hot}} \right) \right)$$

The variable, E_{hot} is the laser energy that has been coupled into hot electrons. The analysis assumed x-rays are generated and attenuated in the stainless steel layer, which was approximated as 18% Cr, 8% Ni and 74% iron with a $<Z>$ of 25.84. The temperatures were between 16.8 and 18 keV and are very consistent for the four shots. The total emitted x-ray energy for each shot is found by integrating the fit spectra above 20 keV. The total energy in 4π recorded by the FFLEX was found to be very small and less than 90 J for photon energies > 20 keV. The data are summarized in Table V.

VIII. X-RAY SPECTRAL MEASUREMENTS

Time integrated spectra were recorded with Super Snout II (SS-II) [41], an elliptically curved Bragg crystal spectrometer. SS-II has four independent spectral channels with overlapping energies spanning from 6 to 16 keV, with a varying spectral resolving power, E/Δ E,

from 100 to 400 for millimeter scale sources. The entrance aperture for each pentaerythritol (PET) crystal is comprised of a 100 μm wide slit, with its length parallel to the plane of dispersion, enabling 1D imaging of the plasma at 4x magnification, for the standoff distance between the target and aperture used for these experiments. Data were recorded onto a SR (super-resolution) image plate. The SS-II energy-dependent absolute intensity response is determined by the convolution of integrated reflectivity measurements of the curved PET crystals [56], the SR image plate sensitivity and fade correction as reported by Maddox *et al.* [57], and the known transmissions for the filters. The filters are chosen to keep the incident flux below the image plate saturation level. SS-II was mounted in the polar DIM 0-0 and viewed the plasma from the top LEH, co-centered with the target's axis.

Figure 12 shows the time and spatially integrated spectra measured for N120627 recorded on SS-II channel 1 (black: 5.8-10.1 keV) and channel 2 (blue: 6.4-11.2 keV). Channel 3 (7.2-12.7 keV) is not shown for clarity (shown in Figure 13). Channel 4 (9.3-16.5 keV) measured only the continuum emission and is also not shown. The SS-304 spectrum is dominated by the Fe K-shell emission, with prominent $1s2p \rightarrow 1s^2$ and $1s3p \rightarrow 1s^2$ He-like and $2p \rightarrow 1s$ hydrogen-like resonance and satellite transitions. The same transitions from Ni and $np \rightarrow 1s$ ($n > 3$) in Cr also in this energy range.

Over plotted with the SS-II spectra is the reconstructed spectrum from Dante 1 for shot N120627-002. The absolute scales of the Dante and the SS-II spectra are different as expected. The Dante is a very low resolution system, whereas, the SS-II has a much higher resolution. The high resolution instrument records the individual lines as tall and narrow features. The lower resolution Dante records the same emission as broad and weaker features. The features in the Dante spectrum are more a function of the response functions and not the individual spectra lines. The total area under the recorded features is important, not the peak brightness. The relative agreement between the two instruments between 6 to 8 keV is fair.

IX. CONVERSION EFFICIENCY DISCUSSION

From the reconstructed spectra from both Dante 1 and 2, the estimated total radiated energy and conversion efficiency in the K-shell x-ray region can be determined for these targets. Several assumptions are made in the determination of the values given in Ta-

ble V. First, the photons below 3 keV (M- and L-shell emission) are assumed to be emitted from two Lambertian radiators at the top and bottom ends of the cylindrical target. Second, the photons above 3 keV (mainly K-shell emission and continuum) are assumed to be isotropic. The radiated energy, $E_{(0.050-20keV)}$, can be estimated by $E_{Lambertian(0.050-3keV)}$ x 2 + $E_{Isotropic(3-20keV)}$. The total $XRCE_{(0.050-20keV)}$ for these targets, which is defined as $E_{(0.050-20keV)}/E_{Laser}$, was about 50 to 60%. The total $XRCE_{(0.050-20keV)}$ determined from the Dante 1 spectral reconstruction is more accurate since it had channels with spectral coverage between photon energies of 2 -3.5 keV. The Dante 2 configuration lacked these channels and thus does not give as accurate a spectral reconstruction in this spectral region. The Dante 2 underestimates the total energy.

The $XRCE_{(5-9keV)}$ is $E_{(5-9keV)}/E_{Laser}$ which includes the emission from the K-shell of Cr and Ni as well as that from the dominant Fe. The average $E_{(5-9keV)}$ is quite large at 31.9±1. and 31.6±1 kJ as determined from Dante 1 and 2, respectively. The repeatability for the four shots was excellent. About 6.8±0.3% of the E_{Laser} was turned into K-shell radiation! The LASNEX simulations predicted $XRCE_{(5-9keV)} = 5.25\%$ and is fairly close to the measurement. We have found little sensitivity of the simulated x-ray emission to variations in the di-electronic recombination rate; whether or not we force energy conservation on each computational cycle; or whether or not there is strict consistency between the radiation field and the matter. There were approximations made in the numerical solution of the conservation of energy equation that may explain why the code underestimates the total K-shell emission; this is undergoing further study and will be addressed in future work.

The creation of a bright K-shell source in the > 5 keV photon energy range does require specific conditions to maximize the conversion efficiency. The simulations must calculate the plasma conditions correctly to obtain an accurate XRCE. One of the most critical parameters is the plasma electron temperature, T_e. The T_e needs to be high enough to ionize a sufficient fraction of the ions into either the He-like or H-like ionization state. The ionization potential, I_P, of Li-like into He-like iron is 2.04 keV. To ionize the He-like ion requires 8.82 keV. To get a significant fraction of the ions in the He-like state only requires a plasma temperature of a few keV. The simulations indicate that the average ionization state $< Z(iron) >$ for the NIF experiments is 24.3 to 24.9. Also critical are the populations of the upper states that feed the ~7 keV K-shell emission lines. An electron temperature higher than 2 keV is needed to have a sufficient number of energetic electrons (> 7 keV) to collisionally excite

the ions into the upper 2p state of the He-like or H-like transition. This is illustrated in the normalized output K-shell power density, P_k, plotted in Figure 14. P_k can be approximated by balancing the collisional excitation rate with the radiative decay rate. All the K-shell emission is assumed to be from ions at the same ionization level as discussed by Back *et al.* [1]. Then by including induced emission and absorption in the energy-balance equation from [58], P_k, can be written as

$$P_k \sim \frac{n_e^2}{<Z>} \frac{e^{(-h\nu/kT_e)}}{(kT_e)^{1/2}}$$

The $h\nu$ is the photon energy for the iron K-shell, and k is the Boltzmann constant. The electron density, n_e, is $\sim$0.2 n_c as determined from the simulations. The simulated time history of the maximum T_e of the NIF shot is shown in the Figure 15. The P_k is a strong function of T_e at the NIF conditions.

With this in mind, the measured line ratios from the SS-II spectrum given in Figure 16, may provide a clue to the differences between the time integrated LASNEX simulated and measured Fe K-shell XRCE. We see that the measured intensity ratio of the Fe Ly_α to He_α lines is less than the simulated ratio. This ratio is largely a function of the plasma electron temperature. The high-resolution spectral data suggest that the simulation is not getting the plasma electron temperature quite right. Is there more (or less) non-local thermal conduction than what we are calculating? Are there hot spots or cold spots in the plasma because of beam-to-beam power imbalances? Are approximations made in the calculations responsible for the discrepancies? These are all questions for further study.

The NIF XRCE can be compared with the recent OMEGA experiments by Pérez, et. al [33]. We expect the SS-304 K-shell XRCE to be about 2-3 times higher for the NIF targets than for the SS-304 lined cavities shot on the OMEGA laser. As mentioned above, the reported K-shell yield was $\sim$23 J/sr or $\sim$250 J which is a $XRCE_{(6.5-8.5keV)}$ of 1.6 - 2.2%. The targets were heated with 20 TW with 20 kJ of 3ω laser light in a 1 ns square in time pulse. The OMEGA targets were 2 mm in diameter and 2 mm in height. The SS-304 lining had thickness of 1, 3 or 5 μm. A typical spectrum from one of the Omega targets is compared with the NIF spectra in Figure 13. The Omega target had a 3 μm thick SS-304 lining. The time integrated spectra from Omega was recorded with a convex crystal spectrometer, the Henway [59, 60]. The Fe Ly_α to He_α line ratio can be seen to be significantly less in the Omega spectra. The T_e in the Omega experiment was reported to be 2$\pm$0.2 keV which is

much lower than that achieved in the NIF experiment.

The input power density was approximately the same for the OMEGA and NIF experiments since NIF delivered ∼7.5 times the power into ∼8 times the volume compared to the OMEGA experiments. However, NIF heated the plasma to ∼2-3 times higher electron temperatures compared to the OMEGA laser. The simulated T_e on the targets' axis as a function of time during the stainless steel cavity experiments on NIF and OMEGA is plotted in Figure 15. The plasma in the NIF target had an axial $T_e > 5$ keV during much of the laser heating of the target. Whereas, the OMEGA target barely achieved a temperature of 3 keV. The P_k on axis for both the NIF and the OMEGA SS-304 experiments are indicated in Figure 14. The greater XRCE on NIF was a result of the higher achievable T_e.

The pulsed power Z machine at Sandia National Laboratory has an ongoing effort to produce bright x-ray sources from nested stainless steel wire array targets. Recently results by Ampleford *et al.* [61] have reported a high conversion efficiency from low mass (1-2 mg) stainless steel wires in a 70 mm in diameter double nested wire array. The x-ray pulse is roughly Gaussian in time with a full width half maximum duration of 2-3 ns which is comparable with the NIF x-ray emission reported here. The nested wire array emitted a peak power of ∼30 TW for photon energies of greater than 5 keV. This results in about 80 kJ of K-shell energy. The reported peak electron temperature is ∼5 keV. For the NIF experiments, the peak K-shell power is about 11 TW or about one-half that reported in the nested wire array targets. The total yield is about 2.5 less for the NIF shots.

We note that the NIF targets were heated with ∼460 kJ of laser energy. NIF is capable of delivering a factor of ∼3 more energy to these targets, which is a fraction of the 1.8 MJ of laser energy available. The NIF targets were heated to only 7 keV which is less than the 12 keV needed for optimal K-shell emission. With more laser energy, higher plasma temperatures can be created. Brighter K-shell sources as well as higher XRCE are most likely achievable.

X.   CONCLUSION

We report on the results of a cylindrical, stainless steel high XRCE K-shell source at the NIF laser. The XRCE in the 5 - 9 keV spectral range was measured to be 6.8±0.3%. The sources were 4.1 mm diameter 4 mm tall hollow epoxy tubes having a 50 μm thick wall

supporting a tube of 3.0 to 3.5 μm thick stainless steel. Photometrically calibrated spectral measurements determined that the targets produced ~ 31 kJ of K-shell x-ray yield with a peak power of ~ 11 TW. Gated x-ray images were taken to confirm the volumetric emission in the K-shell predicted by LASNEX simulations. The LASNEX simulations predicted a $\mathrm{XRCE}_{(5-9keV)} = 5.25\%$ and is fairly close to the measurement. We conclude that the $> 3x$ increase in XRCE from the NIF targets compared to the OMEGA targets of similar design is due to a $> 2x$ increase in peak electron temperature in the targets.

XI. ACKNOWLEDGMENTS

[1] C. A. Back, J. Grun, C. Decker, L. J. Suter, J. Davis, O. L. Landen, R. Wallace, W. W. Hsing, J. M. Laming, U. Feldman, M. C. Miller, and C. Wuest, Phys. Rev. Lett. **87** 275003 (2001).

[2] J. D. Lindl, P. Amendt, R. L. Berger, S. G. Glendinning, S. H. Glenzer, S. W. Haan, R. L. Kauffman, O. L. Landen, and L. J. Suter, Phys. of Plasmas **11** 339 (2004).

[3] H-S Park, K. T. Lorenz, R. M. Cavallo, S. M. Pollaine, S. T. Prisbrey, R. E. Rudd, R. C. Becker, J. V. Bernier, and B. A. Remington, Phys. Rev. Lett. **104** 135504 (2010).

[4] C. A. Coverdale, C. Deeney, P. D. LePell, B. Jones, J. Davis, R. W. Clark, J. P. Apruzese, J. W. Thornhill, and K. G. Whitney, Phys. Plasmas **15**, 023107 (2008).

[5] J. M. Soures, R. L. McCrory, C. P. Verdon, A. Babushkin, R. E. Bahr, T. R. Boehly, R. Boni, D. K. Bradley, D. L. Brown, R. S. Craxton, J. A. Delettrez, W. R. Donaldson, R. Epstein, P. A. Jaanimagi, S. D. Jacobs, K. Kearney, R. L. Keck, J. H. Kelly, T. J. Kessler, R. L. Kremens, J. P. Knauer, S. A. Kumpan, S. A. Letzring, D. J. Lonobile, S. J. Loucks, L. D. Lund, F. J. Marshall, P. W. McKenty, D. D. Meyerhofer, S. F. B. Morse, A. Okishev, S. Papernov, G. Pien, W. Seka, R. Short, M. J. Shoup, M. Skeldon, S. Skupsky, A. W. Schmid, D. J. Smith, S. Swales, M. Wittman, and B. Yaakobi, Phys. Plasmas **3** 2108 (1996).

[6] E. I. Moses, R. E. Bonanno, C. A. Haynam, R. L. Kauffman, B. J. MacGowan, and R. W. Patterson, Jr., Eur. Phys. J. D **44** 215 (2007).

[7] C. A. Haynam, P. J. Wegner, J. M. Auerbach, M. W. Bowers, S. N. Dixit, G. V. Erbert, G. M. Heestand, M. A. Henesian, M. R. Hermann, K. S. Jancaitis, K. R. Manes, C. D. Marshall, N. C. Mehta, J. Menapace, E. Moses, J. R. Murray, M. C. Nostrand, C. D. Orth, R. Patterson, R. A. Sacks, M. J. Shaw, M. Spaeth, S. B. Sutton, W. H. Williams, C. C. Widmayer, R. K. White, S. T. Yang, and B. M. Van Wonterghem, Appl. Opt. **46** 3276 (2007).

[8] O. L. Landen, D. R. Farley, S. G. Glendinning, L. M. Logory, P. M. Bell, J. A. Koch, F. D. Lee, D. K. Bradley, D. H. Kalantar, C. A. Back, and R. E. Turner, Rev. Sci. Instrum. **72** 627 (2001).

[9] B. E. Blue, J. F. Hansen, and H. F. Robey, Rev. Sci. Instrum. **75** 3989 (2004).

[10] R. Tommasini, H.-S. Park, P. Patel, B. Maddox, S. Le Pape, S. P. Hatchett, B. A. Remington, M. H. Key, N. Izumi, M. Tabak, J. Koch, O. L. Landen, D. Hey, A. MacKinnon, J. Seely, G. Holland, L. Hudson, and C. Szabo, AIP Conf. Proc. **926** 248 (2007).

[11] H.-S. Park, B. R. Maddox, E. Giraldez, S. P. Hatchett, L. T. Hudson, N. Izumi, M. H. Key, S. Le Pape, A. J. MacKinnon, A. G. MacPhee, P. K. Patel, T. W. Phillips, B. A. Remington, J. F. Seely, R. Tommasini, R. Town, J. Workman, and E. Brambrink, Phys. Plasmas **15** 072705 (2008).

[12] K. B. Fournier, J. Celeste, V. Rekow, D. R. Bopp, M. J. May, J. H. Fisher, R. Horton, C. D. Newlander, P. Jenkins, and K. Trautz, Rev. Sci. Instrum. **81** 075113 (2010)

[13] K. A. Flippo, J. L. Kline, F. W. Doss, E. N. Loomis, M. Emerich, B. Devolder, T. J. Murphy, K. B. Fournier, D. H. Kalantar, S. P. Regan, M. A. Barrios, E. C. Merritt, T. S. Perry, I. L. Tregillis, L. Welser-Sherrill and J. R. Fincke, Rev. Sci. Instrum. **85** 093501 (2014).

[14] B. E. Blue, S. V. Weber, S. G. Glendinning, N. E. Lanier, D. T. Woods, M. J. Bono, S. N. Dixit, C. A. Haynam, J. P. Holder, D. H. Kalantar, B. J. MacGowan, A. J. Nikitin, V. V. Rekow, B. M. Van Wonterghem, E. I. Moses, P. E. Stry, B. H. Wilde, W. W. Hsing, and H. F. Robey, Phys. Rev. Lett. **94** 095005 (2005).

[15] O. L. Landen *et al.*, Eur. Phys. J. D **44** 273 (2007).

[16] A. B. Reighard, S. G. Glendinning, P. E. Young, W. W. Hsing, M. Foord, M. Schneider, K. Lu, T. Dittrich, R. Wallace, and C. Sorce, Rev. Sci. Instrum. **79** 10E915 (2008).

[17] J. Workman and G. A. Kyrala, in Applications of X Rays Generated from Lasers and Other Bright Sources II, edited by G. A. Kyrala and J.-C. J. Gauthier SPIE, San Diego, **4504** pp. 168179 (2001).

[18] C. A. Back, J. Davis, J. Grun, L. J. Suter, O. L. Landen, W. W. Hsing, and M. C. Miller, Phys. Plasmas **10** 2047 2003.

[19] K. B. Fournier, C. Constantin, J. Poco, M. C. Miller, C. A. Back, L. J. Suter, J. Satcher, J. Davis, and J. Grun, Phys. Rev. Lett. **92** 165005 (2004).

[20] K. Fournier, C. Constantin, G. Gregori, M. Miller, C. Back, L. Suter, J. Davis, and J. Grun, AIP Conf. Proc. **730** 223 (2004).

[21] K. Fournier, C. Constantin, C. Back, L. Suter, H. Chung, M. Miller, D. Froula, G. Gregori, S. Glenzer, E. Dewald, and O. Landen, J. Quant. Spectrosc. Radiat. Transf. **99** 186 (2006).

[22] K. B. Fournier, J. H. Satcher, M. J. May, J. F. Poco, C. M. Sorce, J. D. Colvin, S. B. Hansen, S. A. MacLaren, S. J. Moon, J. F. Davis, F. Girard, B. Villette, M. Primout, D. Babonneau, C. A. Coverdale, and D. E. Beutler, Phys. Plasmas **16** 052703 (2009).

[23] M. Tanabe, H. Nishimura, S. Fujioka, K. Nagai, N. Yamamoto, Z. Gu, C. Pan, F. Girard, M. Primout, B. Villette, D. Brebion, K. B. Fournier, A. Fujishima, and K. Mima, Appl. Phys. Lett. **93** 051505 (2008).

[24] F. Girard, J. P. Jadaud, M. Naudy, B. Villette, D. Babonneau, M. Primout, M. C. Miller, R. L. Kauffman, L. J. Suter, J. Grun, and J. Davis, Phys. Plasmas **12** 092705 (2005).

[25] D. Babonneau, M. Primout, F. Girard, J. P. Jadaud, M. Naudy, B. Villette, S. Depierreux, C. Blancard, G. Faussurier, K. B. Fournier, L. Suter, R. Kauffman, S. Glenzer, M. C. Miller, J. Grun, and J. Davis, Phys. Plasmas **15** 092702 (2008).

[26] F. Girard, M. Primout, B. Villette, P. Stemmler, L. Jacquet, D. Babonneau, and K. B. Fournier, Phys. Plasmas **16** 052704 (2009); **18** 079901 (2011).

[27] M. A. Barrios, S. P. Regan, K. B. Fournier, R. Epstein, R. Smith, A. Lazicki, R. Rygg, D. E. Fratanduono, J. Eggert, H.-S. Park, C. Huntington, D. K. Bradley, O. L. Landen, and G. W. Collins, Rev. Scien. Instr. **85** 11D502 (2014)

[28] J. Workman and G. A. Kyrala, Rev. Sci. Instrum. **72** 678 (2001).

[29] J. Denavit and D. W. Phillion, Phys. Plasmas **1** 1971 1994.

[30] D. Babonneau, M. Primout, F. Girard, J. P. Jadaud, M. Naudy, B. Villette, S. Depierreux, C. Blancard, G. Faussurier, K. B. Fournier, L. Suter, R. Kauffman, S. Glenzer, M. C. Miller, J. Grun, and J. Davis, Phys. Plasmas **15** 092702 (2008).

[31] K. B. Fournier, M. J. May, J. D. Colvin, J. O. Kane, M. Schneider, E. Dewald, C. A. Thomas, S. Compton, R. E. Marrs, J. Moody, E. Bond, P. Michel, J. H. Fisher, C. D. Newlander, and

J. F. Davis, Phys. Plasmas **17**, 082701 (2010).

[32] M. Primout, L. Jacquet, D. Babonneau, F. Girard, B. Villette, J.-P. Jadaud, M. Naudy, P. Stemmler, and J. L. Ulmer, J. Phys.: Conf. Ser. **112** 042051 (2008).

[33] F. Pérez, J. J. Kay, J. R. Patterson, J. Kane, B. Villette, F. Girard, C. Reverdin, M. May, J. Emig, C. Sorce, J. Colvin, S. Gammon, J. Jaquez, J. H. Satcher, Jr., K. B. Fournier, Phys. of Plasmas **19** 083101 (2012).

[34] K. B. Fournier, M. J. May, J. D. Colvin, M. A. Barrios, J. R. Patterson and S. P. Regan, Phys Rev E **88** 033104 (2013).

[35] K. M. Campbell, F. A. Weber, E. L. Dewald, S. H. Glenzer, O. L. Landen, R. E. Turner, and P. A. Waide, Rev. Sci. Instrum. **75**, No 10, 3768- 3771 (2004).

[36] E. L. Dewald, K. M. Campbell, R. E. Turner, J. P. Holder, O. L. Landen, S. H. Glenzer, R. L. Kauffman, L. J. Suter, M. Landon, M. Rhodes, and D. Lee, Rev. Sci. Instrum. **75** 3759 (2004).

[37] H. N. Kornblum, R. L. Kauffman, and J. A. Smith, Rev. Sci. Instrum. **57** 2179 (1986).

[38] J. A. Oertel, R. Aragonez, T. Archuleta, C. Barnes, L. Casper, V. Fatherley, T. Heinrichs, R. King, D. Landers, F. Lopez, P. Sanchez, G. Sandoval, L. Schrank, P. Walsh, P. Bell, M. Brown, R. Costa, J. Holder, S. Montelongo, and N. Pederson, Rev. Sci. Instrum. **77** 10E308 (2006).

[39] D. H. Froula, *et al.*, Rev. Sci. Instrum. **75** 4168 (2004).

[40] A. J. Mackinnon, T. McCarville, K. Piston, C. Niemann, G. Jones, I. Reinbachs, R. Costa, J. Celeste, G. Holtmeier, R. Griffith, R. Kirkwood, B. MacGowan, S. H. Glenzer, and M. R. Latta, Rev. Sci. Instrum. **75** 4183 (2004).

[41] S. P. Regan, M.A. Barrios, K.B. Fournier, J.D. Kilkenny, J. Emig, C. Bailey, P. Bell, D.K. Bradley, M. Bedzyk, R. Epstein, B.A. Hammel, M.J. Haugh, W. Hising, R. Jungquist, O.L. Landen, D.W. Larson, T. Ma., J. Magoon, D.D. Meyerhofer, M.J. Shoup, L.J. Suter, and D. Rowley, Be Submitt. RSI (n.d.).

[42] C. A. Haynam, P. J. Wegner, J. M. Auerbach, M. W. Bowers, S. N. Dixit, G. V. Erbert, G. M. Heestand, M. A. Henesian, M. R. Hermann, K. S. Jancaitis, K. R. Manes, C. D. Marshall, N. C. Mehta, J. Menapace, E. Moses, J. R. Murray, M. C. Nostrand, C. D. Orth, R. Patterson, R. A. Sacks, M. J. Shaw, M. Spaeth, S. B. Sutton, W. H. Williams, C. C. Widmayer, R. K. White, S. T. Yang, and B. M. Van Wonterghem, Applied Optics, **46**, No. 16, 3276-3303

(2007).

[43] S. N. Dixit, M. D. Feit, M. D. Perry, and H. T. Powell, Opt. Lett. **21**, 17151717 (1996).

[44] G. B. Zimmerman and W. L. Kruer, Comments Plasma Phys. Controlled Fusion **2** 51 (1975).

[45] H. A. Scott and S. B. Hansen, High Energy Density Phys. **6** 39 (2010).

[46] L. Spitzer, "Physics of Fully Ionized Gases", Wiley, New York, N.Y., 1962.

[47] J. D. Colvin, K. B. Fournier, M. J. May, and H. A. Scott, Phys. Plasmas **17** 073111 (2010).

[48] J. D. Colvin, K. B. Fournier, J. Kane, S. Langer, M. J. May, and H. A. Scott, High Energy Density Phys. **7** 263 (2011).

[49] M. J. May,b K. Widmann, C. Sorce, H.-S. Park, and M. Schneider, Rev. Sci. Instrum. **8** 10E505 (2010).

[50] M. J. May, J. R. Patterson, C. Sorce, K. Widmann, K. B. Fournier, and F. Pérez, Rev. Sci. Instrum. **83** 10E117 (2012).

[51] H. F. Robey, T. S. Perry, H.-S. Park, P. Amendt, C. M. Sorce, S. M. Compton, and K. M. Campbell, J. P. Knauer, Phys of Plasmas **12**, 072701 (2005).

[52] J. W. McDonald, R. L. Kauffman, J. R. Celeste, M. A. Rhodes, F. D. Lee, L. J. Suter, A. P. Lee, J. M. Foster, and G. Slark, Rev. Sci. Instrum. **75** 3753 (2004).

[53] C. L. Wang, Rev. Sci. Instrum. **52** 1317 (1981).

[54] E.L. Dewald, et. al., Rev. Sci. Instrum. 81, 10D938 (2010)

[55] W. L. Kruer, The Physics of Laser Plasma Interactions (Westview, Boulder, CO, 2003).

[56] M.J. Haugh, S.P. Regan, K.D. Jacoby, P.W. Ross, J. Magoon, M.A. Barrios, J.A. Emig, M.J. Shoup, and K.B. Fournier, Rev. Sci. Instrum. **83** 10E122 (2012).

[57] B.R. Maddox, H.S. Park, B.A. Remington, N. Izumi, S. Chen, C. Chen, G. Kimminau, Z. Ali, M.J. Haugh, and Q. Ma, Rev. Sci. Instrum. **82** 023111 (2011).

[58] Y. B. Zeldovich and Y. P. Raizer, Physics of Shock Waves and High-Temperature Hydrodynamic Phenomena (Academic, New York, 1967).

[59] L.N. Koppel, J.D. Eckels, UCRL-79781, October 1977.

[60] M.J. May, M.B. Schneider, S.B. Hansen, H.-K. Chung, D.E. Hinkel, H.A. Baldis, C. Constantin, High Energy Density Physics **4** 7887 (2008).

[61] D. J. Ampleford, C. A. Jennings, B. Jones, S. B. Hansen, M. E. Cuneo, C. A. Coverdale, M. C. Jones, T. M. Flanagan, M. Savage, W. A. Stygar, M. R. Lopez, J. P. Apruzese,) J. W. Thornhill, J. L. Giuliani, and Y. Maron Phys. Plasmas **20** 103116 (2013).
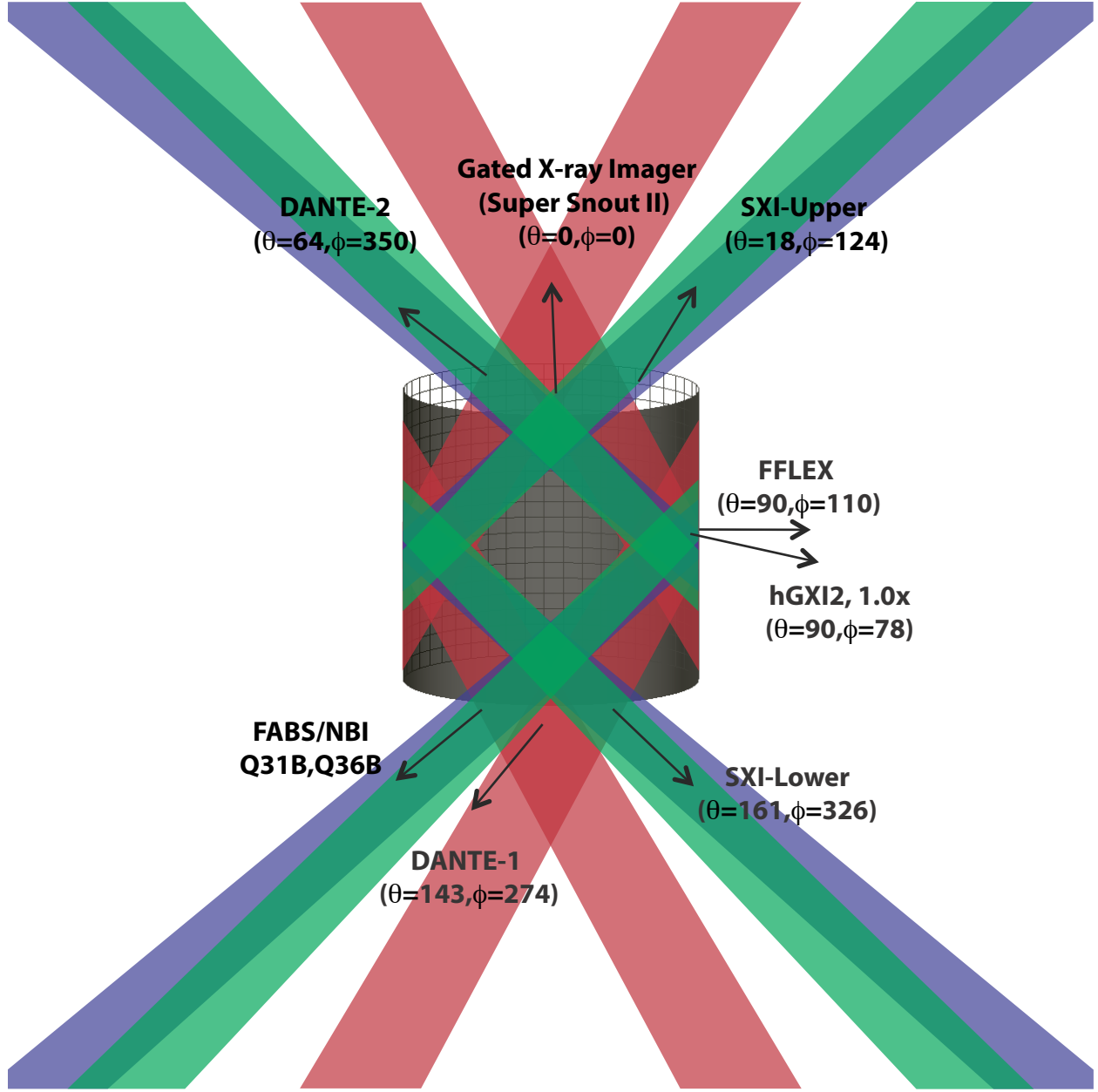
FIG. 1. (Color Online) Overview of the NIF laser configuration, SS-304 cylindrical target and diagnostic locations for the target shots. The 30° quads (in red), the 44.5° quads (in green) and the 50° quads (in blue) are shown. The NIF chamber (θ, ϕ) coordinates of each diagnostic are given.
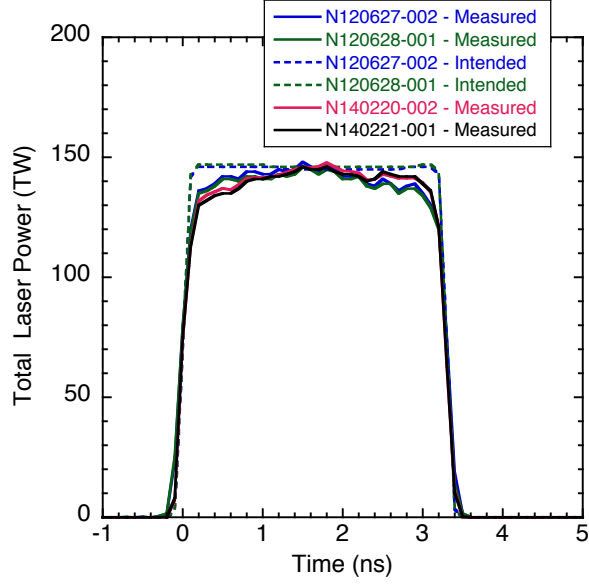
FIG. 2. (Color Online) Intended and measured laser power for four NIF shots: N120627-002, N120628-001, N140220-002 and N140221-001.
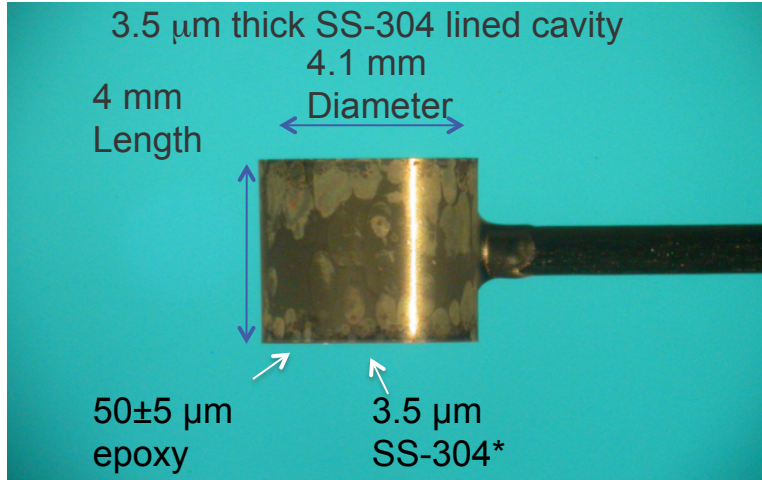

FIG. 3. (Color Online) Mounted SS-304 Cavity Target (Fe 70%, Cr 17%, Ni 9%, Mo 1%, Si 1.5% and Mn 1.5%).
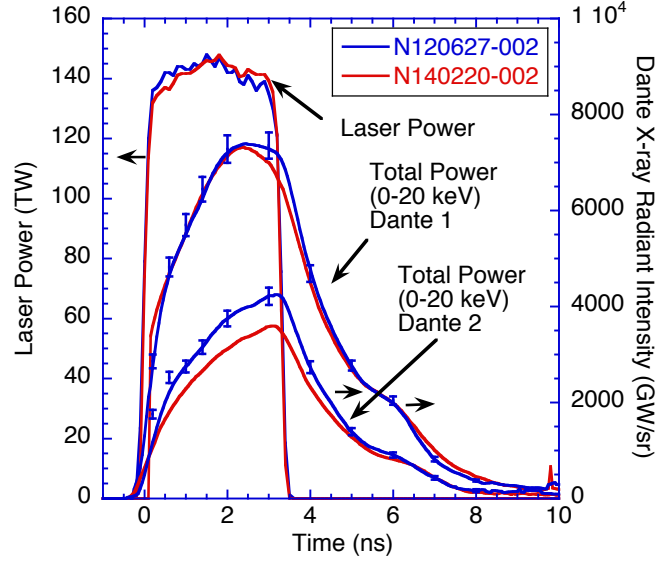
FIG. 4. (Color Online) Laser power and reconstructed total radiant intensity as a function of time for Dante 1 and Dante 2 for the N120627-002 and N140220-002 target shots.
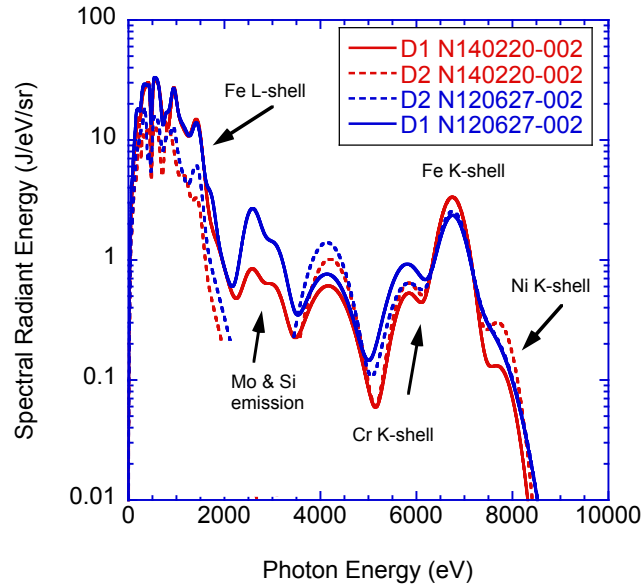

FIG. 5. (Color Online) Reconstructed Spectra for Dante 1 and Dante 2 for the N120627-002 and N140220-002 target shots.
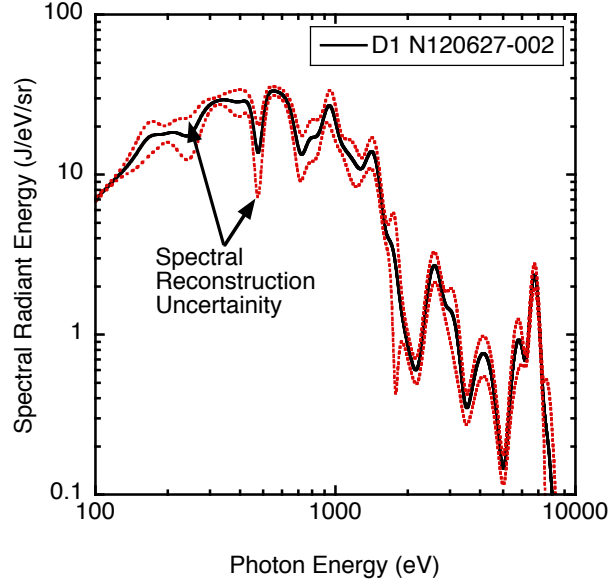
FIG. 6. (Color Online) Reconstructed Spectra for Dante 1 for the N120627-002 with the one sigma uncertainties of the reconstruction.
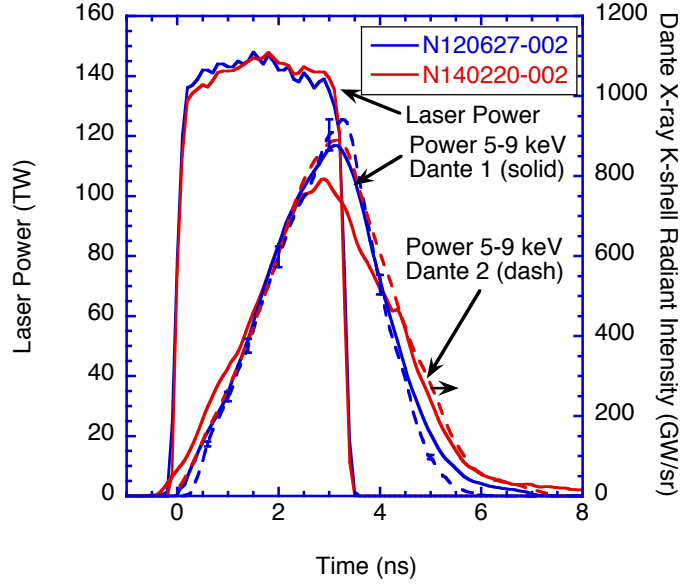

FIG. 7. (Color Online) Laser power and reconstructed K-shell radiant intensity as a function of time for Dante 1 and Dante 2 for the N120627-002 and N140220-002 target shots.
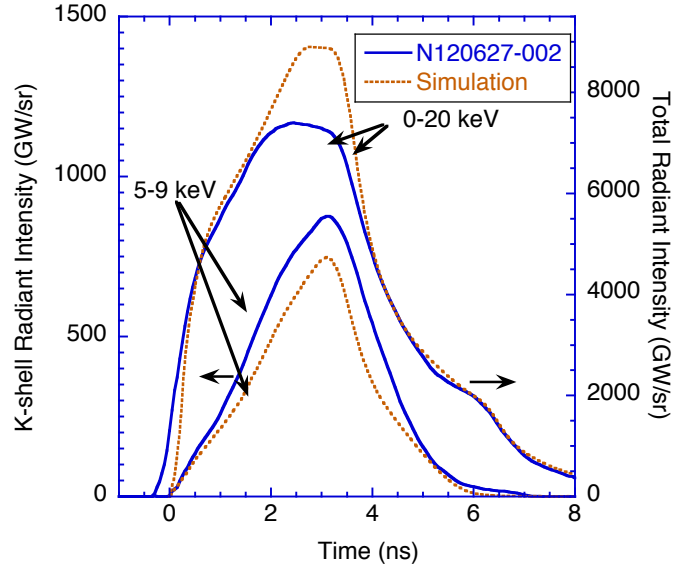
FIG. 8. (Color Online) Total and K-shell (5 - 9 keV) radiant intensity as a function of time from Dante 1 and LASNEX simulation for N120627-002.
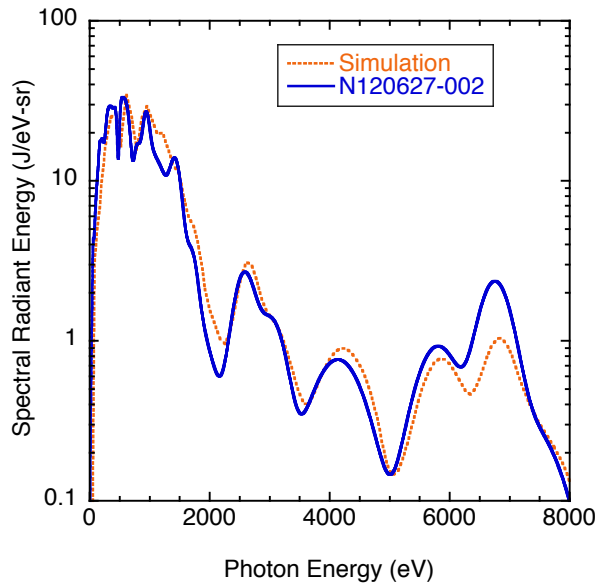

FIG. 9. (Color Online) Reconstructed Spectra from Dante 1 and LASNEX simulation for N120627-002.

Simulation

1.00 ns   2.00 ns   3.00 ns   4.00 ns

N120627-002

1.03 ns   2.04 ns   3.10 ns   4.15 ns

Vertical

4.1 mm

N120628-001

0.94 ns   1.97 ns   3.03 ns   4.08 ns
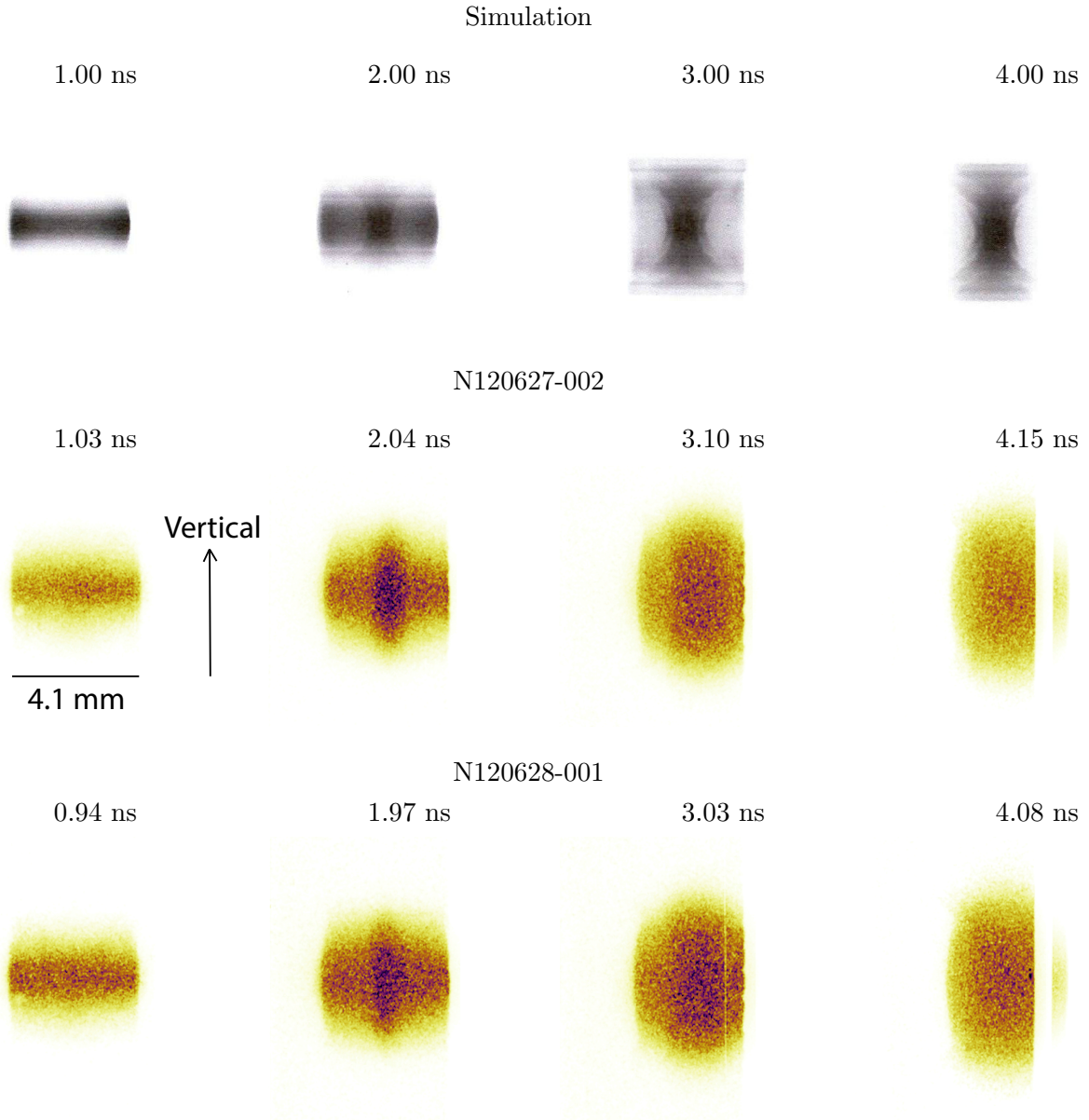
FIG. 10. (Color Online) Gated x-ray images for NIF shots N120627-002 and N120628-001 compared with simulations having an equatorial target view.
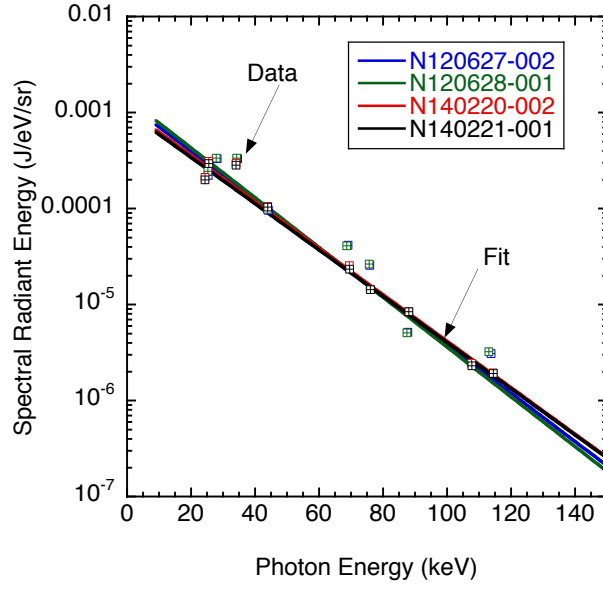
FIG. 11. (Color Online) FFLEX spectra for shots N120627-002, N120628-001, N140220-002 and N140221-001.
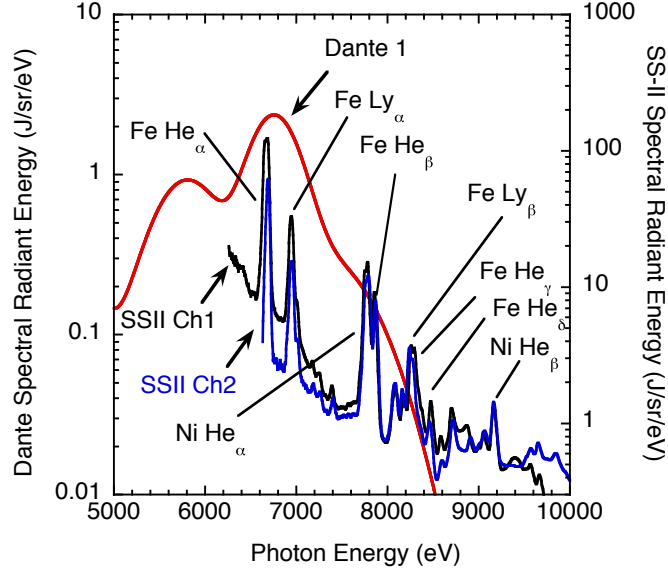
FIG. 12. (Color Online) Time integrated high resolution spectra from the SS-II as viewed from the axis of the cylinder compared with the Dante 1 data for N120627-002.
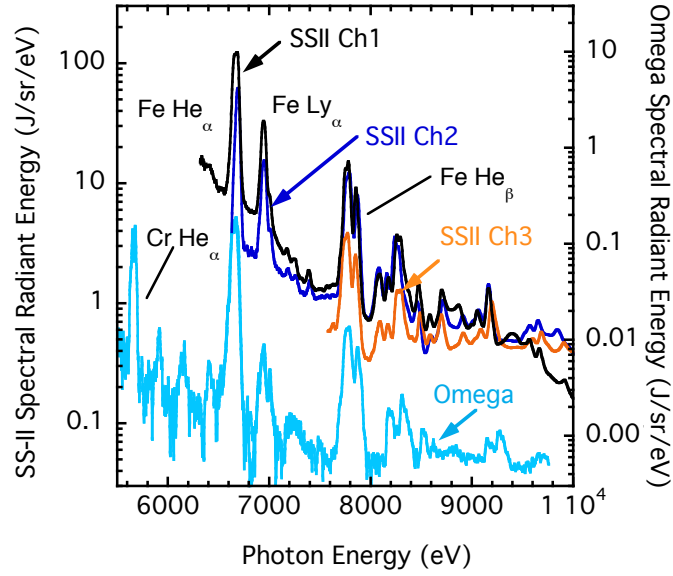
FIG. 13. (Color Online) Comparison of time integrated high resolution spectra from the NIF and Omega stainless steel cavity experiments. The SS-II spectra from channels 1, 2 and 3 are plotted for shot N120627-002. The Omega spectra was recorded with the Henway crystal spectrometer.

FIG. 14. (Color Online) Normalized K-shell power density as a function of electron temperature.

FIG. 15. (Color Online) Calculated maximum T_e versus time for the SS-304 cavity targets in the NIF experiments and the OMEGA experiments.

FIG. 16. (Color Online) Time integrated high resolution spectra for N120627-002 from the SS-II scaled to the Dante total power compared with the time integrated LASNEX simulation.
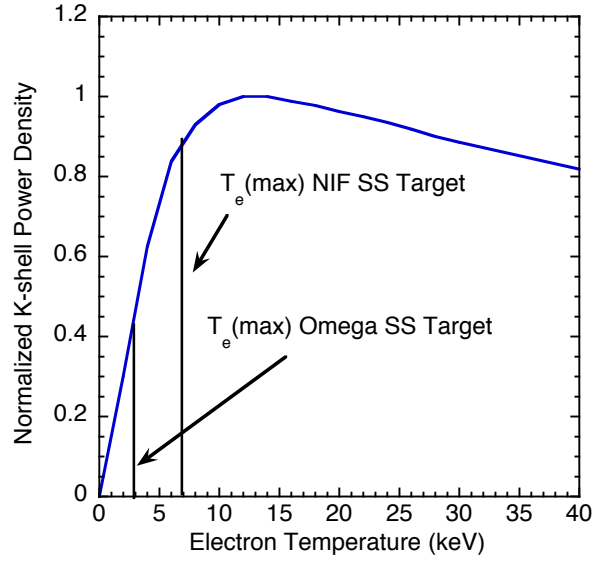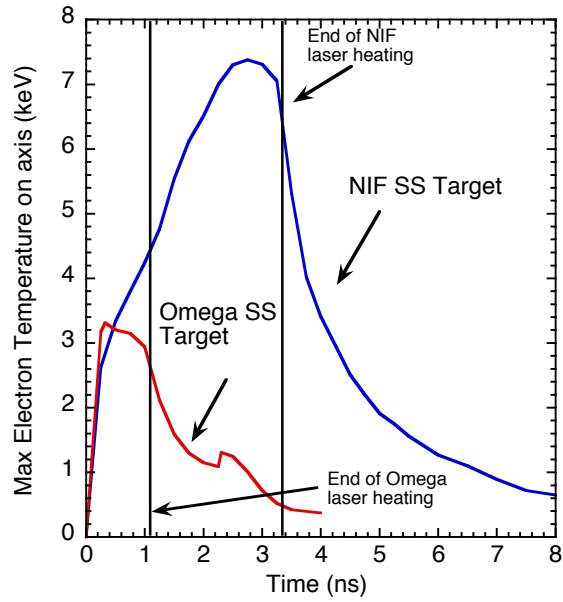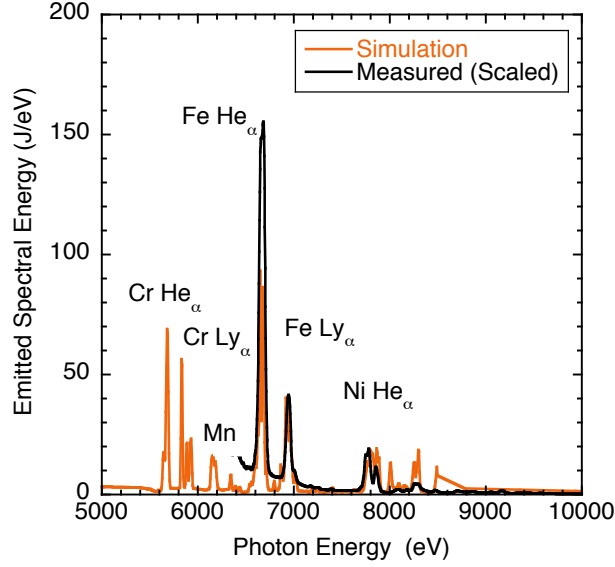
TABLE I. Summary of the laser parameters for the stainless steel target shots.

Shot	N120627-002	N120628-001	N140220-002	N140221-001
E(Laser) Intended (kJ)	500	500	500	500
E(Laser) Measured (kJ)	466.3	461.9	463.3	461.1
E(Laser Outer Cone) Measured (kJ)	371.6	366.2	379.6	375.0
E(Laser Inner Cone) Measured (kJ)	93.5	95.7	83.4	86.1
Wavelength(Laser Outer Cone) (nm)	350.850	350.850	350.950	350.950
Wavelength(Laser Inner Cone) (nm)	351.093	351.093	350.950	350.950
P(Laser) Intended (TW)	150	150	150	150
P(Laser) Measured (TW)	144.5	143.2	145.1	143.9
Laser Pulse Length (ns)	3.3	3.3	3.3	3.3
Nominal Energy per Beam (kJ)	3.125	3.125	3.125	3.187
Number of Beams	156	156	156	152
Number of 30° Quads	8	8	7	7
Dropped 30° Quads	-	-	Q44B	Q44B
Number of 44.5° Quads	16	16	16	15
Dropped 44.5° Quads	-	-	-	Q43B
Number of 50° Quads	15	15	16	16
Dropped 50° Quads	Q26B	Q26B	-	-

TABLE II. Pointing and CPPs for the laser beams used in the target shots. Coordinates are referenced from the target chamber center, which is also the geometric center of the targets.

Cone	Lower Hemisphere	Upper Hemisphere	x (mm)	y (mm)	z (mm)	CPPs	Major axis diameter (μm)	minor axis diameter (μm)
Inner cone	30°	150°	0	0	±2.8	Rev 1.0 Rev1a Inner Cone 2ω	1648	1180
Outer cone	44.5°	135.5°	0	0	±1.5	Rev3 Outer Cone 2ω	1270	734
Outer cone	50°	130°	0	0	±1.5	Rev 1.0 Rev1 Outer Cone 2ω	1186	686

TABLE III. Metrology of the SS-304 cavity targets

Shot	N120627-002	N120628-001	N140220-002	N140221-001
Target	FeKshell-A-01	FeKshell-A-02	FeKShell-C-01	FeKShell-C-02
Epoxy Wall Thickness	55 μm	50 μm	53 μm	50 μm
Inside Diameter of SS-304 Tube	4090 μm	4093 μm	4102 μm	4111 μm
SS-304 Thickness	3.5 μm	3.5 μm	3.0 μm	3.0 μm
Length of Cylinder	3990 μm	3950 μm	3984 μm	3992 μm

TABLE IV. Configurations of Dante 1. Columns are the channel number, the filters present in the channel, the number of each type of filter present, the type of XRD used, the Ta wire grid if present, a soft x-ray mirror with angle of grazing incidence if present, the energy range over which that channel had sensitivity, and the solid angle subtended by that channel.

Channel	Filter	Qty	XRD	Ta Grids	Mirror	Nominal Energy Range Center (eV)	Nominal Energy Range Width (eV)	Solid Angle x10^{-7}
1	Al 0.8 μm	2	Cr	-	7°, B$_4$C	58.5	16.6	6.026
2	B 0.5 μm + CH 0.4 μm	2	Al	-	5°, amorphous C	166.9	27.4	5.929
3	Lexan 2.0 μm	2	Al	-	3.5°, SiO$_2$	248.8	46.1	5.786
4	V 1.0 μm	2	Ni	-	2.5°, SiO$_2$	477.5	46.8	5.603
5	Ti 13 μm	2	Cr	-	-	4137.7	827.5	6.514
6	Ni 10 μm	2	Cr	-	-	7330.7	925.0	6.514
7	Mg 5.0 μm + Zn 1.0 μm + CH 0.1 μm	1	Ni	Yes	-	942.3	98.1	6.514
8	Mg 11 μm	2	Ni	Yes	-	1182.8	158.4	6.514
9	Al 10 μm	2	Ni	Yes	-	1430.5	174.4	6.514
10	Si 10 μm	2	Al	-	-	1712.7	156.3	6.514
11	Cu 0.55 μm	2	Al	Yes	-	828.9	137.6	6.514
12	Saran 22 μm	3	Al	-	-	2573.4	334.2	6.514
13	Ag 2.2 μm	2	Al	-	-	3024.2	437.0	6.514
14	Co 1.0 μm + Co 0.4 μm + CH 0.2 μm	1	Al	Yes	-	709.3	92.8	6.514
15	Mn 13.2 μm + Ni 1.8 μm	2	Ni	-	-	5805.2	690.8	6.514
16	Fe 15 μm	2	Ni	-	-	6750.4	500.6	6.514
17	Ti 0.5 μm	2	Al	Yes	2.5°, SiO$_2$	400.0	70.7	5.603
18	Fe 15 μm	1	Ni	-	-	5740.9	1148.1	17.73

TABLE V. Summary of the energetics of the stainless steel target shots.

Shot	N120627-002		N120628-001		N140220-002		N140221-001	
Dante	Dante 1	Dante 2	Dante 1	Dante 2	Dante 1	Dante 2	Dante 1	Dante 2
View Angle	37°	64°	37°	64°	37°	64°	37°	64°
Total (E_{photon} = 0.05-20 keV)								
Simulated Radiant Energy (kJ/sr)	32.9	18.1	32.2	18.2	-	-	-	-
Measured Radiant Energy (kJ/sr)	32.5±1.5	17.1±0.74	32.6±1.5	17.7±0.74	31.5±1.4	14.6±0.6	31.8±1.4	14.5±0.6
Measured Energy (Lambertian corrected) (kJ)	270.±12	239.±10	271.±12	247.±10	264±12	203.±10	267.±12	202.±10
Measured Conversion Efficiency	57.9±2.7%	51.3±2.3%	58.7±2.6%	54.7±2.3%	56.9±2.6%	43.9±2.2%	57.9±2.6%	43.9±2.2%
L-shell (E_{photon} = 0.05-2 keV)								
Simulated Radiant Energy (kJ/sr)	28.6	14.7	27.8	14.6	-	-	-	-
Measured Radiant Energy (kJ/sr)	27.2±1.3	13.3±0.59	27.3±1.3	13.9±0.6	26.9±1.3	10.9±0.5	27.2±1.3	10.8±0.5
Measured Energy (Lambertian corrected) (kJ)	214.±9.9	191.±8.5	215.±10.	199.±8.5	212.±10.	156.±7.2	214.±10.	155.±7.2
(E_{photon} = 5 - 9 keV)								
Measured Radiant Energy (kJ/sr)	2.52±0.12	2.40±0.12	2.51±0.12	2.47±0.12	2.57±0.12	2.74±0.12	2.59±0.12	2.72±0.12
Measured Energy (kJ)	31.7±1.5	30.2±1.5	31.5±1.5	31.0±1.5	32.2±1.5	34.4±1.5	32.5±1.5	34.1±1.5
Measured Conversion Efficiency	6.79±0.3%	6.47±0.3%	6.82±0.3%	6.73±0.3%	6.97±0.3%	7.40±0.3%	7.06±0.3%	7.41±0.3%
Simulated Conversion Efficiency	5.24%	5.24%	5.17%	5.17%	-	-	-	-
Backscatter	31B (30°)		31B (30°)		31B (30°)		31B (30°)	
	SBS	SRS	SBS	SRS	SBS	SRS	SBS	SRS
NBI (J)	359±70	249±70	399±80	356±70	409.7±80	314.2±60	458.8±90	355.5±70
FABS (J)	16±3	29±6	19±4	43.±8	25.2±5	41.1±8	32.7±7	49.3±10
total (J)	375.15	277.48	417.75	399.44	434.96	355.22	491.43	404.79
Total Backscatter (kJ)	39±8		46±9		30±6		33±7	
% of Energy Backscattered	8.3±1.5%		9.9±2%		6.4±1.3%		7.2±1.5%	
FFLEX Fit T_{hot} (keV)	17.2±3.0		16.8±3.0		17.9±3.0		18.±3.0	
FFLEX Energy (J) [> 20 keV]	83.1±2.9		87.5±3.2		78.6±2.5		75.0±2.5	